Atomic configurations of dislocation core and twin boundaries in 3*C*-SiC studied by high-resolution electron microscopy

C. Y. Tang,[1] F. H. Li,[1,*] R. Wang,[2] J. Zou,[3] X. H. Zheng,[4] and J. W. Liang[4]
[1]*Beijing National Laboratory for Condensed Matter Physics, Institute of Physics, Chinese Academy of Sciences, P.O. Box 603, Beijing 100080, China*
[2]*Department of Materials Physics and Chemistry, University of Science and Technology Beijing, Beijing 100083, China*
[3]*School of Engineering and Centre for Microscopy and Microanalysis, The University of Queensland, Brisbane QLD 4072, Australia*
[4]*R&D Center for Optoelectronic Technology, Institute of Semiconductors, Chinese Academy of Sciences, P.O. Box 912, Beijing 100083, China*
(Received 20 November 2006; published 10 May 2007)

The defects in 3*C*-SiC film grown on (001) plane of Si substrate were studied using a 200 kV high-resolution electron microscope with point resolution of 0.2 nm. A posterior image processing technique, the image deconvolution, was utilized in combination with the image contrast analysis to distinguish atoms of Si from C distant from each other by 0.109 nm in the [110] projected image. The principle of the image processing technique utilized and the related image contrast theory is briefly presented. The procedures of transforming an experimental image that does not reflect the crystal structure intuitively into the structure map and of identifying Si and C atoms from the map are described. The atomic configurations for a 30° partial dislocation and a microtwin have been derived at atomic level. It has been determined that the 30° partial dislocation terminates in C atom and the segment of microtwin is sandwiched between two 180° rotation twins. The corresponding stacking sequences are derived and atomic models are constructed according to the restored structure maps for both the 30° partial dislocation and microtwin. Images were simulated based on the two models to affirm the above-mentioned results.

DOI: 10.1103/PhysRevB.75.184103 PACS number(s): 68.37.Lp, 42.30.Wb

I. INTRODUCTION

Semiconductor nanostructures[1,2] have been a global research focus in recent decades due to their nature of being building blocks for future nanoelectronics and nanooptoelectronics.[3] As a consequence, it is vitally important to understand their fine atomic configuration of defects in these nanostructures as defects can significantly degrade their physical and mechanical properties. Silicon carbide (SiC) thin film is a kind of promising two-dimensional semiconducting nanomaterial for high-power and high-frequency devices because of its wide band gap, high breakdown field, and high thermal conductivity. As one of the polytypes of SiC, 3*C*-SiC has been investigated much less than its counterparts, such as 4*H*-SiC and 6*H*-SiC, although 3*C*-SiC films grown on Si substrate are commonly considered to be able to combine the excellent properties of SiC with the mature Si technology.[4] Owing to a large lattice mismatch (20%) and a significant difference in thermal expansion coefficients between Si and SiC, a high density of defects such as misfit dislocations,[5] stacking faults (SFs),[6] microtwins,[7,8] and antiphase boundaries[9,10] is frequently introduced into the 3*C*-SiC films grown on Si substrate. It is believed that these defects may cause serious damage to electronic devices based on SiC. To study the structure of defects, high-resolution electron microscopy (HREM) is considered as a very effective technique.

In general, high-resolution electron microscope images are strongly modulated by the contrast transfer function (CTF) of an electron microscope. Only the images taken near the Scherzer defocus condition[11] for a sufficiently thin specimen may reflect the real crystal structure with a resolution restricted to the point resolution of the microscope. It was reported that the structures and defects in SiC can be directly observed at atomic level with high-voltage high-resolution electron microscopes.[12,13] Recently, a new kind of medium-voltage field-emission gun (FEG) microscope with the spherical aberration corrector and monochromator has been developed, which is able to provide a point resolution of 0.07 nm.[14] Hence, the structure of 3*C*-SiC with the atomic resolution should be attainable with such microscopes. A third way for the same purpose is to restore the structure map of examined crystal with the resolution approaching the information limit of a FEG microscope by means of posterior image processing techniques, such as exit wave reconstruction[15–17] and image deconvolution.[18–20] So far these techniques have been successfully applied to images taken with 200 and 300 kV microscopes.

Originally the image deconvolution method was developed for deriving unknown structures from a single image with an arbitrary defocus usually taken from a non-FEG microscope. It is based on the pseudo-weak-phase object approximation (pseudo-WPOA).[21] The direct method developed in x-ray crystallography[19] and the principle of maximum entropy[20] were utilized to determine the defocus value. Though the structure resolution attained by image deconvolution is generally constrained by the resolution of the electron microscope, it can be enhanced to the diffraction resolution limit by combining the corresponding diffraction data and performing the phase extension.[22,23] So far a number of crystal structures including incommensurately modulated structures[24–31] have been determined. An alternate type of work dealing with image deconvolution is developed to determine defect structures in crystals whose structures in

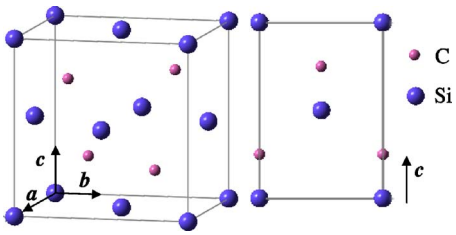

FIG. 1. (Color online) Structure model of 3*C*-SiC (left) and its [110] projection (right).

perfect regions are known before.[32–37] In the latter case, the resolution of deconvoluted images was improved up to the information limit of the microscope. For this it is important to improve the image quality by reducing the dynamical scattering effect via the diffraction amplitude correction.[33–37] The present work belongs to the second category, in which the image deconvolution combined with the diffraction amplitude correction was utilized to investigate the atomic configurations for a partial dislocation core and for twin boundaries in a 3*C*-SiC film grown on the Si substrate.

In the following, a short paragraph dealing with the experiment and structure model of 3*C*-SiC is given in Sec. II. In Sec. III, the utilized image processing methods and a practical image contrast theory in HREM are briefly introduced. An experimental image is shown in Sec. IV, from which three regions were selected to make a detailed analysis in Secs. V–VII. Section V concentrates on how to distinguish atoms Si and C in the image when the microscope resolution is insufficient to resolve atoms individually. The results obtained in this section serve as the basis for Secs. VI and VII to determine the core structure of a 30° partial dislocation and the structure of twin boundaries, respectively, at atomic level.

II. EXPERIMENT AND STRUCTURE MODEL

The 3*C*-SiC film was grown on Si (001) substrate by the atmosphere pressure chemical vapor deposition technique. Silane (SiH_4) and propane (C_3H_8) were used as the precursors of Si and C, respectively. Prior to the deposition of the film, a "carbon buffer layer" is formed by exposing the silicon surface to propane, typically at 1300 °C. The ⟨110⟩ cross-section specimen for high-resolution electron microscope observation was prepared by Ar-ion-beam thinning. The microscopic observation was performed using a JEM 2010 microscope with C_s=0.5 mm and the point resolution of 0.194 nm.

The crystal 3*C*-SiC has a cubic structure of zinc-blende type with lattice parameter a=0.436 nm. Since for such structures the majority of dislocations in cubic semiconductors is along the ⟨110⟩ directions and planar defects often lie on {111} planes, it is appropriate to study these defects using high-resolution electron microscope images projected in the ⟨110⟩ directions. Figure 1 shows the structure models of 3*C*-SiC. Atoms of Si and C are grouped in pairs in the [110] projected structure. The distance between the two atoms in the pair is 0.109 nm. Usually, such atomic pairs are named "dumbbells" in HREM.

III. IMAGE CONTRAST INTERPRETATION AND IMAGE DECONVOLUTION

A. Image contrast changes with crystal thickness for different atomic numbers

In HREM, the weak-phase object approximation (WPOA) is widely used to interpret why the image can intuitively reflect the crystal structure. According to the WPOA the image intensity is expressed as

$$I(\boldsymbol{r}) = 1 + 2\sigma\varphi(\boldsymbol{r}) * \mathcal{F}^{-1}[T(H)], \tag{1}$$

where $\sigma=\pi/\lambda U$, λ is the wavelength and U the accelerating voltage of electrons, and $*$ and $\mathcal{F}^{-1}$ are operators of convolution and inverse Fourier transform, respectively. $\varphi(\boldsymbol{r})$ is the projected potential distribution function (PPDF) and $T(H)$ the CTF. $\boldsymbol{r}$ and $\boldsymbol{H}$ are coordinate vectors in the real space and reciprocal space, respectively. At the Scherzer focus condition, Eq. (1) approximately turns into

$$I(\boldsymbol{r}) = 1 - 2\sigma\varphi(\boldsymbol{r}). \tag{2}$$

Equation (2) indicates that the image intensity is linear to the PPDF of the structure. Such images are named structure images where all atoms appear black.

However, the WPOA is valid only for extremely thin samples and cannot indicate how the image contrast changes with the crystal thickness. Providing a modification and supplement to the WPOA, the pseudo-WPOA (Ref. 21) declares that the Scherzer focus image can be expressed more practically as

$$I(\boldsymbol{r}) = 1 - 2\sigma\varphi'(\boldsymbol{r}) \tag{3}$$

and

$$\varphi'(\boldsymbol{r}) = \varphi(\boldsymbol{r}) + \Delta\varphi(\boldsymbol{r}), \tag{4}$$

Here, the function $\varphi'(\boldsymbol{r})$ is named pseudo-PPDF. The increment $\Delta\varphi(\boldsymbol{r})$ depends on the crystal thickness and contains the second-order terms of $\varphi(\boldsymbol{r})$. Hence, the secondary scattering effects are included, to some extent, in Eq. (3). It was demonstrated that as long as the crystal thickness is below a critical value, the peak positions for $\varphi'(\boldsymbol{r})$ would be exactly the same as the peak positions for $\varphi(\boldsymbol{r})$, i.e., the atomic positions. The difference between $\varphi'(\boldsymbol{r})$ and $\varphi(\boldsymbol{r})$ is only in the peak heights. When the crystal is as thin as a weak-phase object, Eq. (3) will degenerate to Eq. (2). With the increase of crystal thickness, the relative contrast alters such that the darkness of light atoms increases more rapidly than that of heavy atoms, and with the further increase of crystal thickness, light atoms may appear darker in the image than heavy atoms. Such feature of the image contrast is essential to recognizing Si and C atoms in images. This will be discussed in detail in Secs. V–VII.

B. Validity of WPOA for crystal structure determination

According to the pseudo-WPOA, the critical thickness t_c depends on the electron wavelength λ and the atomic number Z_h of the heaviest constituent atoms. The smaller the values of λ and Z_h, the larger the value of t_c. For 200 kV micro-

scopes, t_c is typically of several nanometers. It is well known that such value of crystal thickness fits those for taking structure images of good quality. The pseudo-PPDF can be understood as the PPDF of an imaginary crystal isomorphic to the examined real crystal. As compared with the atoms in the real crystal, in the imaginary isomorphic crystal, the fictitious heavy atoms will appear lighter and vice versa. Therefore, the image contrast of a Scherzer focus image is linear to the pseudo-PPDF when the crystal thickness is below the critical value. At or above the critical thickness, the heaviest atoms in the crystal will either have no contrast or have a reverse contrast so that the one-to-one correspondence between the image and the PPDF will no longer exist. This implies that Eq. (1) is valid for crystal structure determination only if the crystal thickness is below the critical value.

C. Principle of image deconvolution

The principle of image deconvolution and diffraction amplitude correction has been described in previous publications[19,20,32–34] and is introduced briefly here. Assume that the crystal thickness is below the critical value and hence Eq. (1) is valid. After replacing the function $\varphi(\boldsymbol{r})$ by $\varphi'(\boldsymbol{r})$, the Fourier transform (FT) of Eq. (1) yields

$$i(\boldsymbol{H}) = \delta(\boldsymbol{H}) + 2\sigma F'(\boldsymbol{H})T(H), \tag{5}$$

where $F'(\boldsymbol{H})$ is the FT of $\varphi'(\boldsymbol{r})$ (named the pseudo-structure factor). When the transmitted beam $\delta(\boldsymbol{H})$ is ignored, Eq. (5) can be rearranged into

$$F'(\boldsymbol{H}) = \frac{i(\boldsymbol{H})}{2\sigma T(H)}. \tag{6}$$

$T(H)$ can be calculated if the spherical aberration coefficient C_s, defocus value Δf, and defocus spread due to the chromatic aberration D are known. Thus, $F'(\boldsymbol{H})$ and the corresponding pseudo-PPDF $\varphi'(\boldsymbol{r})$ can be obtained.

The image defocus is first determined by matching the FT of an amorphous image area (named Thon diffractogram[38]) with CTF curves calculated for various values of Δf, and then is refined in the course of image deconvolution. The detailed process of defocus refinement is described in Ref. 36.

D. Principle of diffraction amplitude correction

It should be emphasized that the practical sample can hardly be a weak phase object, and hence the dynamical scattering effect is inevitable. A method for correcting diffraction amplitude $F'(\boldsymbol{H})$ was developed[33] to reduce the dynamical scattering effect by using the formulas

$$F'^{\mathrm{cor}}_{\boldsymbol{H}} = K_{\boldsymbol{H}} \sum_i F'_{\boldsymbol{H}i} \tag{7}$$

and

$$K_{\boldsymbol{H}} = \frac{|F(\boldsymbol{H})|}{|\sum_i F'_{\boldsymbol{H}i}|}. \tag{8}$$

In Eqs. (7) and (8), K_H is the correction coefficient which is a constant within each reflection but varies for different reflections, $F'_{\boldsymbol{H}i}$ denotes the amplitude value in the ith pixel for reflection $\boldsymbol{H}$ inside the corresponding window, and $F(\boldsymbol{H})$ denotes the structure factor of the perfect crystal. The physical meaning of the method is forcing the integral amplitude of each reflection to be equal to the corresponding structure factor amplitude of the perfect crystal. The final deconvoluted image is obtained by inverse Fourier transforming the diffractogram consisting of $F'^{\mathrm{cor}}(\boldsymbol{H})$.

Circular windows[33] or elliptical windows[34] were utilized for Fourier filtering and for collecting the integral amplitude of reflections. Employing circle windows for point and line defects and elliptical windows for planar defects is recommended.

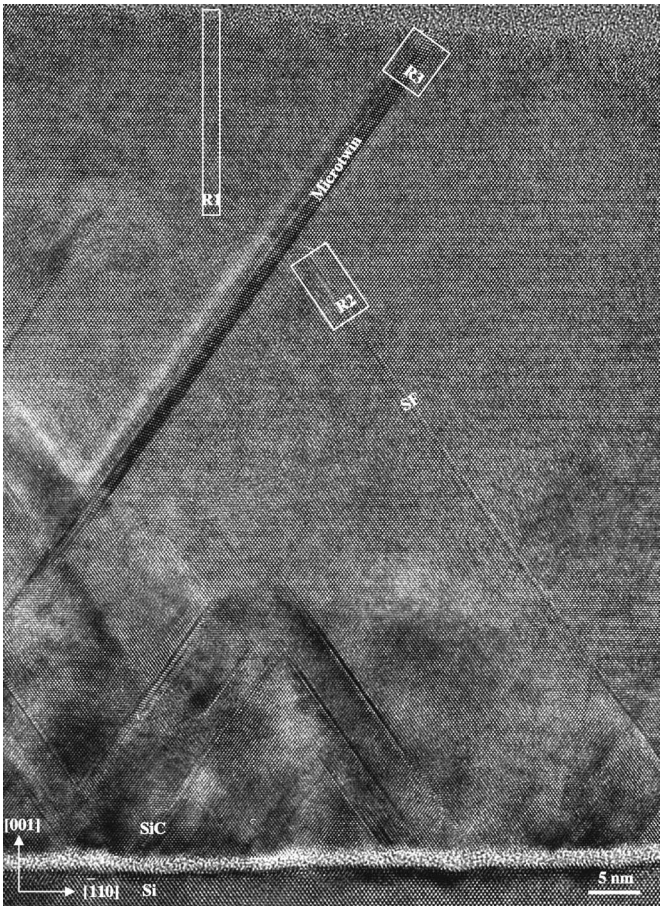

FIG. 2. [110] high-resolution electron microscope image of 3C-SiC grown on Si substrate.

IV. EXPERIMENTAL IMAGE AND DEFOCUS DETERMINATION

Figure 2 shows the experimental image of 3C-SiC/Si projected in the [110] direction taken near the Scherzer defocus. It is a lattice image showing the lattice periods and defects rather than a structure image. It is well known that Schockley 60° dislocations are frequently introduced into the basal {111} plane of SiC, owing to the lattice parameter mismatch of SiC and Si. Usually, an extended 60° dislocation will dissociate into a couple of partial dislocations, the 30° and 90°

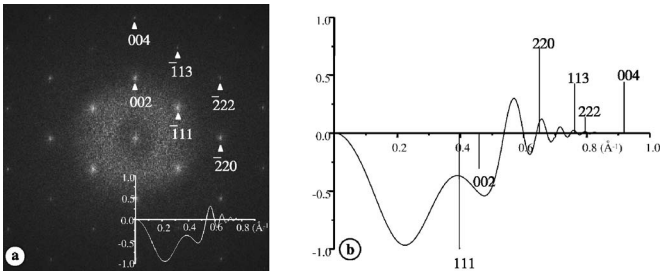

FIG. 3. (a) Thon diffractogram obtained from the top edge in Fig. 2 with the CTF curve matched on the bottom right. (b) The CTF curve calculated for $\Delta f=-46$ nm, $C_s=0.5$ mm, and $D=6$ nm together with the six independent reflections of 3*C*-SiC.

ones with a SF in between. When several couples of partial dislocations are arranged in order, a microtwin comes into formation.[39,40] A typical partial dislocation core with a single layer SF and a microtwin with five stacking layers are framed in rectangles labeled with R2 and R3, respectively.

The FT of a selected image area including both the amorphous and crystalline regions on the top of Fig. 2 is given in Fig. 3(a) where the Thon diffractogram[38] consisting of diffuse rings and the diffractogram consisting of arrayed reflections which come from the crystalline image area are superimposed. The image defocus was determined by matching the CTF curves calculated for different trial values of Δf with the contrast profile of Thon diffractogram. It has been found that the CTF curve calculated for U (accelerating voltage)=200 kV, $C_s=0.5$ mm, $D=6$ nm, and $\Delta f=-46$ nm fits the Thon diffractogram the best [see the inset on the bottom right of Fig. 3(a)]. The accurate value of Δf was obtained by refinement in the course of image deconvolution.

Figure 3(b) is the magnified CTF curve. The positions of six independent reflections 111, 002, 220, 113, 222, and 004 for the [110] projection of SiC are indicated with segments of different lengths representing the relative value of structure factor for the corresponding reflection. It is seen that all reflections other than 111 and 002 are beyond the scope of the microscope's point resolution. Owing to the rapid damping of CTF in high frequency, amplitudes for reflections 220 and 113 are seriously attenuated and the reflections 222 and 004 are almost cut off. It is reasonable to consider that the faint reflections 222 and 004 in Fig. 3(a) mainly come from the secondary scattering. In the next three sections, all the results and the related arguments are evolved from the image shown in Fig. 2.

V. DISTINGUISHING SILICON AND CARBON ATOMS

As shown in Fig. 1, Si and C atoms are grouped into pairs, named dumbbells, in the ⟨110⟩ projected structure of SiC, and the distance between the two atoms in the dumbbell is 0.109 nm which equals the reciprocal of spatial frequency for reflection 004. To reveal atomic columns of Si and C individually with correct distance, the image should contain the structure information contributed by all diffracted waves at least within the scattering angles up to those for 004 and $00\bar{4}$. However, according to the argument given in Sec. IV,

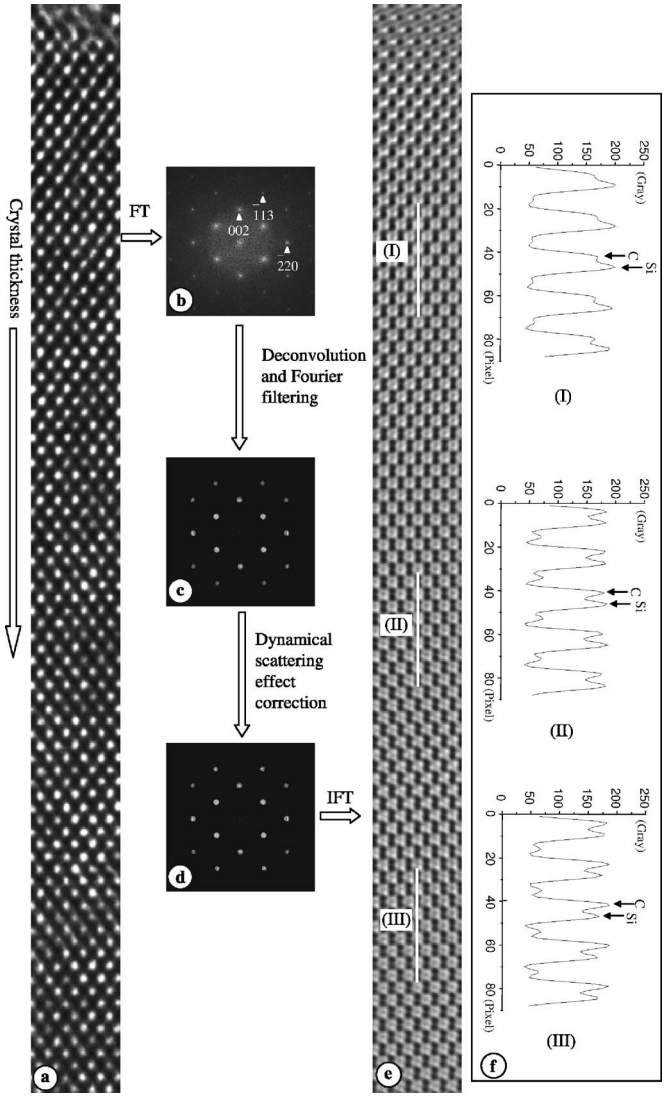

FIG. 4. (a) Magnified micrograph of region R1 shown in Fig. 2, (b) diffractogram obtained by Fourier transforming (a), (c) diffractogram obtained from (b) after Fourier filtering and deducting CTF modulation, (d) diffractogram obtained from (c) after diffraction amplitude correction, (e) deconvoluted image, and (f) contrast profiles of dumbbells for regions I, II, and III, respectively.

only four independent reflections 111, 002, 220, and 113 in the diffractogram can reasonably be utilized. Fortunately, for the diamond as well as zinc-blend structures, the two atoms in the dumbbell can reveal separately in the deconvoluted image as far as the contribution of reflection 113 and its equivalents are included, though the distance between the two atoms will be slightly longer than the correct value owing to the insufficient structure information. This is in accordance with the simulated images for such structures when the contributions of reflections 004 and $00\bar{4}$ are ignored.

At first, the image deconvolution and diffraction amplitude correction were applied to the thin perfect region labeled R1 given in Fig. 2. The magnified micrograph for region R1 is shown in Fig. 4(a). The crystal thickness increases from the top to bottom as indicated by the arrow. Three different diffractograms are shown in Figs. 4(b)–4(d). Figure

4(b) is a direct FT of Fig. 4(a), where reflections 111, 002, 220, and 113 are visible. The value of Δf was determined roughly to be −46 nm and later refined as −46.5 nm through a series of Δf_{trial} in the range of −42 to −49 nm with a focus step of 0.5 nm. Figure 4(c) is obtained from Fig. 4(b) after Fourier filtering and CTF modulation deduction with the transmitted beam omitted. Subsequently, the diffraction amplitudes were corrected for Fig. 4(c) to reduce the dynamical scattering effect, and the finally corrected diffractogram is shown in Fig. 4(d).

The inverse FT of Fig. 4(d) yields the deconvoluted image [Fig. 4(e)], in which each pair of atomic columns Si and C reveals as an individual black dumbbell, with the contrast slightly increasing with the increase of crystal thickness. In order to discern the contrast difference between the two ends in dumbbells, the gray levels were measured for three regions I, II, and III and the contrast profiles are shown in Fig. 4(f). The gray value of 0–255 is assigned to correspond to the contrast change from white to black. The gray level for the upper ends of the dumbbells is lower than, almost equal to, and slightly higher than that for the corresponding lower ends for regions I, II and III, respectively. Because region I is near the amorphous area and hence the thinnest one among the three regions, it is reasonable to approximate region I as a weak-phase object, while regions II and III should be treated as pseudo-weak-phase objects. The contrast of atomic columns Si and C shown in Fig. 4(f) is in agreement with the pseudo-WPOA.[21] The fact that with the increase of crystal thickness the peak height for light atoms goes up quicker than that for heavy atoms corresponds to the case below the critical crystal thickness. Therefore, the upper ends in the dumbbells are recognized as atomic columns of C while the lower ends as Si.

VI. CORE STRUCTURE OF A PARTIAL DISLOCATION

Figure 5(a) is the magnified micrograph for region R2 shown in Fig. 2, where a partial dislocation (the terminated plane is pointed by the arrow and its end is marked with the circle) associated with a SF can be seen. By applying Burgers circuit, the partial dislocation can be determined to be a 30° partial dislocation with a Burgers vector of $1/6\langle 112\rangle$. It is well known that 60° dislocations are generally gliding dislocations that may glide on {111} planes in cubic semiconductors. For the SiC/Si system, these dislocations exist in SiC or at the SiC/Si interface to relieve the misfit strain between the SiC thin film and the Si substrate. Energetically speaking, a 60° dislocation may dissociate into two partial dislocations, a 30° and a 90° with a SF associated with them. This is particularly true for a tensile strained layer grown on a (001) substrate, in which the 90° partial dislocations are located near the strained interface and the 30° partial dislocations are in the film.[41]

Horizontal streaks caused by the SF are seen clearly on both sides of all reflections included in the diffractogram [see the inset in Fig. 5(a)]. The deconvoluted image for Fig. 5(a) with $\Delta f=-47$ nm is shown in Fig. 5(b). The strong streaks seen in the diffractogram inserted in Fig. 5(b) indicate that most of the structural information contributed by the SF is

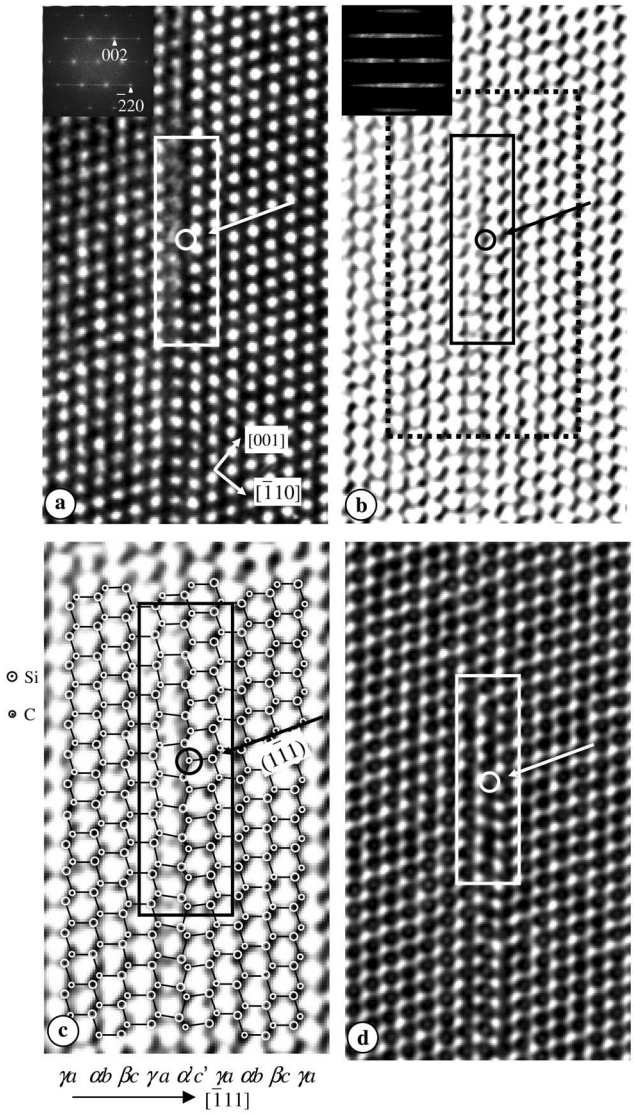

FIG. 5. (a) Magnified micrograph of region R2 shown in Fig. 2, (b) deconvoluted image of (a), (c) magnified picture corresponding to the region inside the dotted rectangle shown in (b) with schematic structure model superimposed, and (d) simulated image with $\Delta f=-47$ nm and $t=5.54$ nm; the solid reference rectangles show the equivalence regions in (a)–(d).

retained. This confirms the right decision of using elliptical windows for the Fourier filtering.[34] In Fig. 5(b), all atoms appear as black and the dumbbells are recognized though not clearly. Figure 5(c) is the magnified picture corresponding to the region inside the dotted rectangle shown in Fig. 5(b). Owing to the insufficient resolution of the microscope, the two ends in the dumbbells are not resolved.

For a 30° partial dislocation, the inserted plane may terminate either in atom Si or atom C, as illustrated in Fig. 6.[42] To identify the terminal atom pointed by the small arrows in Figs. 5(b) and 5(c), the argument of image contrast variation with crystal thickness given in the last section was referred as follows. Since region R2 in Fig. 2 is located farther away from the sample edge than region R1, the thickness of region R2 should be larger than or, at least, similar to that of the

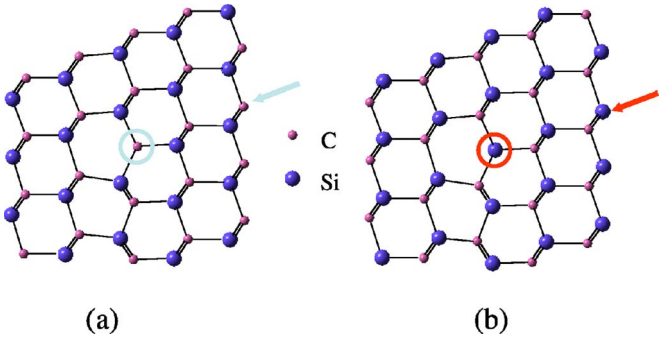

FIG. 6. (Color online) Schematic structure models of 30° partial dislocation terminate in atomic columns of (a) C and (b) Si.

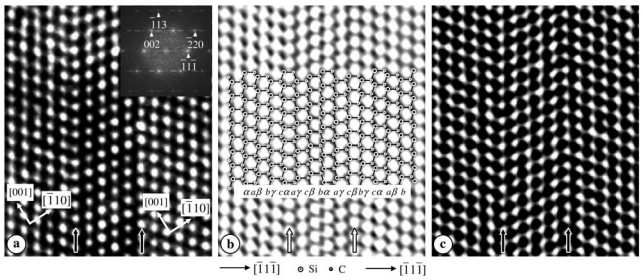

FIG. 8. (a) Magnified micrograph of region R3 shown in Fig. 2, (b) deconvoluted image of (a) with schematic structure model superimposed, and (c) simulated image with $\Delta f=-46.5$ nm and $t=3.08$ nm.

thick part in region R1. Hence, the contrast profile in the segment III shown on the bottom of Fig. 4(f) can be used for Fig. 5(c) to make out that the gray level for Si is lower than that for C. Thus, the smaller ends in the dumbbells correspond to atomic columns of Si, while the bigger ends correspond to the atomic columns of C. Therefore, all Si and C atoms including those pointed by the small arrow can be identified in the deconvoluted image shown in Fig. 5(c) so that it is clear that the partial dislocation terminates in the C atomic column. The atomic configuration of the 30° partial dislocation core and its associated SF was then derived, and the corresponding model is superimposed on the deconvoluted image [see Fig. 5(c)]. The stacking sequence is $\cdots\gamma a\alpha b\beta c\gamma a\alpha' c'\gamma a\alpha b\beta c\gamma a\cdots$, where $\alpha\beta\gamma$ (α') represent atomic layers of Si and abc (c') represent atomic layers of C. Figure 5(d) shows the image simulated based on the model given in Fig. 5(c) with $\Delta f=-47$ nm and the crystal thickness of 5.54 nm, which is in good agreement with the experimental image.

VII. STRUCTURES OF MICROTWIN AND TWIN BOUNDARIES

In 3*C*-SiC, the {111} twins could be either a 180° rotation twin or a mirror reflection twin[43] with the corresponding stacking sequence $\cdots\alpha a\beta b\gamma c\beta b\alpha a\cdots$ or $\cdots\alpha a\beta b\gamma\gamma b\beta a\alpha\cdots$, respectively. The two types of schematic models are shown in Fig. 7. Figure 8(a) is the magnified micrograph for region R3 shown in Fig. 2, which contains a segment of {111} microtwin (marked by two arrows). The corresponding diffractogram is inserted on the top right. Figure 8(b) shows the deconvoluted image of Fig. 8(a) with $\Delta f=-46.5$ nm. Again, atoms appear black and the two atoms in the dumbbells are not resolved clearly. Since this region is near the thin amorphous area, the thickness should be comparable with the top part in Fig. 4(a). Hence, the contrast profile of segment I shown on the top of Fig. 4(f) can be used for Fig. 8(b). Thus, it is reasonable to treat the bigger ends of the dumbbells as atomic columns of Si. The structure model of the microtwin segment together with its boundaries constructed on the basis of the above argument is superimposed on the deconvoluted image [see Fig. 8(b)]. It is seen that the stacking sequence is $\cdots\alpha a\beta b\gamma c\alpha a\gamma c\beta b\alpha a\gamma cb\beta\gamma c\alpha a\beta b\cdots$, and the microtwin segments are sandwiched between two 180° rotation twins. Figure 8(c) shows the image simulated according to the model given in Fig. 8(b) with $\Delta f=-46.5$ nm and the crystal thickness of 3.08 nm. The simulated image agrees well with the experimental image.

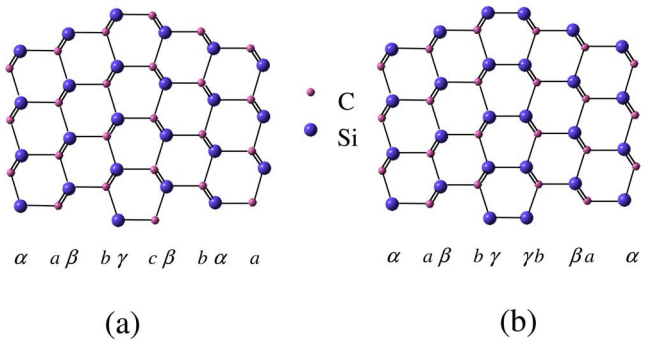

FIG. 7. (Color online) Schematic structure models of (a) 180° rotation twin and (b) mirror reflection twin for 3*C*-SiC.

VIII. CONCLUSIONS

In the present paper, the structures of a 30° partial dislocation core and of twin boundaries in 3*C*-SiC have been determined at atomic level from a single [110] image taken with a conventional 200 kV high-resolution electron microscope of point resolution about 0.2 nm. First, the experimental image that does not directly reflect the crystal structure was transformed into the structure map by image deconvolution. Then, the quality of the restored structure map was improved after weakening the dynamical scattering effect via the diffraction amplitude correction. Here, it is important to preserve the structure information of defects as much as possible by utilizing appropriate windows (circle for point and line defects and elliptical for planar defects) in Fourier filtering and collecting integral reflection amplitudes. Though the point resolution of the restored structure map is about 0.2 nm, the atomic columns of Si and C distant from each other by 0.109 nm have been recognized via the image contrast analysis based on the pseudo-WPOA. This results in the successful determination of defect structures at atomic level that the 30° partial dislocation terminates in C atom and the microtwin segment is sandwiched between two 180° rotation twins. Hence, the corresponding stacking sequences are de-

rived and atomic models are constructed according to the restored structure images for both the 30° partial dislocation and microtwin.

Usually, the defect structures with atomic resolution can be obtained only with a microscope of much higher resolution. The present work indicates that such structure information can also be obtained from images taken with an ordinary popular medium-voltage electron microscope when the posterior processing and contrast analysis are carried out.

ACKNOWLEDGMENT

This project was supported by the National Natural Science Foundation of China (No. 10474122).

*Author to whom correspondence should be addressed. FAX: 86-10-8264-9531. Electronic address: lifh@aphy.iphy.ac.cn

[1] F. M. Ross, R. M. Tromp, and M. C. Reuter, Science **286**, 1931 (1999).
[2] J. Stangl, V. Holy, and G. Bauer, Rev. Mod. Phys. **76**, 725 (2004).
[3] O. G. Schmidt and K. Eberl, IEEE Trans. Electron Devices **48**, 1175 (2001).
[4] H. Nagasawa, T. Kawahara, and K. Yagi, Mater. Sci. Forum **389–393**, 319 (2002).
[5] C. Long, S. Ustin, and W. Ho, J. Appl. Phys. **86**, 2509 (1999).
[6] S. Nutt, D. Smith, H. Jim, and R. Davis, Appl. Phys. Lett. **50**, 203 (1987).
[7] Z. Zekentes, V. Papaioannou, B. Pecz, and J. Stoemenos, J. Cryst. Growth **157**, 392 (1995).
[8] X. H. Zheng, B. Qua, Y. T. Wanga, Z. Z. Daia, J. Y. Hanb, Hui Yanga, and J. W. Liang, J. Cryst. Growth **233**, 40 (2001).
[9] H. Nagasawa, K. Yagi, and T. Kawahara, J. Cryst. Growth **237-239**, 1244 (2002).
[10] P. Pirouz, C. Chorey, and J. Powell, Appl. Phys. Lett. **50**, 221 (1987).
[11] O. Scherzer, J. Appl. Phys. **20**, 20 (1949).
[12] H. Ichinose, Proceedings of the International Kunming Symposium on Microscopy, Kunming, China, 2000 (unpublished), p. 11.
[13] E. Takuma, H. Ichinose, and F. R. Chen, J. Electron Microsc. **51**, 297 (2002).
[14] P. Schlossmacher, A. Thesen, and G. Benner, Eur. Semicond. **27**, 2 (2005).
[15] P. Schiske, Proceedings of the Fourth European Conference on Electron Microscopy, Rome, 1968 (unpublished), p. 145.
[16] D. Van Dyck and M. Op de Beeck, Proceedings of the 12th Congress on Electron Microscopy, Seattle, 1990 (unpublished), Vol. 1, p. 26.
[17] D. Van Dyck and D. M. Op de Beeck, Ultramicroscopy **64**, 99 (1996).
[18] F. H. Li and H. F. Fan, Acta Phys. Sin. **28**, 267 (1979).
[19] F. S. Han, H. F. Fan, and F. H. Li, Acta Crystallogr., Sect. A: Found. Crystallogr. **42**, 353 (1986).
[20] J. J. Hu and F. H. Li, Ultramicroscopy **35**, 339 (1991).
[21] F. H. Li and D. Tang, Acta Crystallogr., Sect. A: Found. Crystallogr. **41**, 376 (1985).
[22] H. F. Fan, Z. Y. Zhong, C. D. Zheng, and F. H. Li, Acta Crystallogr., Sect. A: Found. Crystallogr. **41**, 163 (1985).
[23] H. F. Fan, S. B. Xiong, F. H. Li, Q. Pan, N. Uyeda, and Y. Fujiyoshi, Ultramicroscopy **36**, 361 (1991).
[24] J. J. Hu, F. H. Li, and H. F. Fan, Ultramicroscopy **41**, 387 (1992).
[25] Z. Q. Fu, D. X. Huang, F. H. Li, J. Q. Li, Z. X. Zhao, T. Z. Cheng, and H. F. Fan, Ultramicroscopy **54**, 229 (1994).
[26] B. Lu, F. H. Li, Z. H. Wan, H. F. Fan, and Z. Q. Mao, Ultramicroscopy **70**, 13 (1997).
[27] J. Liu, F. H. Li, Z. H. Wan, H. F. Fan, X. J. Wu, T. Tamura, and K. Tanabe, Mater. Trans., JIM **39**, 920 (1998).
[28] H. Jiang, F. H. Li, and Z. Q. Mao, Micron **30**, 417 (1999).
[29] J. Liu, F. H. Li, Z. H. Wan, H. F. Fan, X. J. Wu, T. Tamura, and K. Tanabe, Acta Crystallogr., Sect. A: Found. Crystallogr. **57**, 540 (2001).
[30] H. B. Wang, H. Jiang, F. H. Li, G. C. Che, and D. Tang, Acta Crystallogr., Sect. A: Found. Crystallogr. **58**, 494 (2002).
[31] S. X. Yang and F. H. Li, Ultramicroscopy **85**, 51 (2000).
[32] W. Z. He, F. H. Li, H. Chen, K. Kawasaki, and T. Oikawa, Ultramicroscopy **70**, 1 (1997).
[33] F. H. Li, D. Wang, W. Z. He, and H. Jiang, J. Electron Microsc. **49**, 17 (2000).
[34] C. Y. Tang and F. H. Li, J. Electron Microsc. **54**, 445 (2005).
[35] D. Wang, F. H. Li, and J. Zou, Ultramicroscopy **85**, 131 (2000).
[36] D. Wang, H. Chen, F. H. Li, K. Kawasaki, and T. Oikawa, Ultramicroscopy **93**, 139 (2002).
[37] D. Wang, J. Zou, W. Z. He, H. Chen, F. H. Li, K. Kawasaki, and T. Oikawa, Ultramicroscopy **98**, 259 (2004).
[38] F. Thon, *Electron Microscopy in Materials Science* (Academic, New York, 1971).
[39] P. Pirouz and J. W. Yang, Ultramicroscopy **51**, 189 (1993).
[40] P. Pirouz, Solid State Phys. **56**, 107 (1997).
[41] J. Zou and D. J. H. Cockayne, J. Appl. Phys. **74**, 925 (1993).
[42] A. T. Blumenau, C. J. Fall, R. Jones, S. Öberg, T. Frauenheim, and P. R. Briddon, Phys. Rev. B **68**, 174108 (2003).
[43] D. B. Holt, J. Phys. Chem. Solids **25**, 1385 (1964).